ARL-TR-7415 • Sep 2015

US Army Research Laboratory

Using the ALEGRA Code for Analysis of Quasi-Static Magnetization of Metals

by Michael Grinfeld, John Niederhaus, and Andrew Porwitzky

NOTICES

Disclaimers

The findings in this report are not to be construed as an official Department of the Army position unless so designated by other authorized documents.

Citation of manufacturer's or trade names does not constitute an official endorsement or approval of the use thereof.

Destroy this report when it is no longer needed. Do not return it to the originator.

ARL-TR-7415 ● SEP 2015

US Army Research Laboratory

Using the ALEGRA Code for Analysis of Quasi-Static Magnetization of Metals

by Michael Grinfeld and Andrew Porwitzky
Weapons and Materials Research Directorate, ARL

John Niederhaus
Center for Computing Research, Sandia National Laboratories

REPORT DOCUMENTATION PAGE

Form Approved
OMB No. 0704-0188

PLEASE DO NOT RETURN YOUR FORM TO THE ABOVE ADDRESS.

1. REPORT DATE *(DD-MM-YYYY)*	2. REPORT TYPE	3. DATES COVERED (From - To)
September 2015	Final	January 2015 - May 2015

4. TITLE AND SUBTITLE
Using the ALEGRA Code for Analysis of Quasi-Static Magnetization of Metals

5a. CONTRACT NUMBER

5b. GRANT NUMBER

5c. PROGRAM ELEMENT NUMBER

6. AUTHOR(S)
Michael Grinfeld, John Niederhaus, and Andrew Porwitzky

5d. PROJECT NUMBER
ABC123

5e. TASK NUMBER

5f. WORK UNIT NUMBER

7. PERFORMING ORGANIZATION NAME(S) AND ADDRESS(ES)
US Army Research Laboratory
ATTN: RDRL-WMP-C
Aberdeen Proving Ground, MD 21005-5066

8. PERFORMING ORGANIZATION REPORT NUMBER
ARL-TR-7415

9. SPONSORING/MONITORING AGENCY NAME(S) AND ADDRESS(ES)

10. SPONSOR/MONITOR'S ACRONYM(S)

11. SPONSOR/MONITOR'S REPORT NUMBER(S)

12. DISTRIBUTION/AVAILABILITY STATEMENT
Approved for public release; distribution is unlimited.

13. SUPPLEMENTARY NOTES
Primary author's email: michael.greenfield4.civ@mail.mil. Sandia National Laboratories is a multi-program laboratory managed and operated by Sandia Corporation, a wholly owned subsidiary of Lockheed Martin Corporation, for the U.S. Department of Energy National Nuclear Security Administration under contract DE-AC04-94AL85000.

14. ABSTRACT
The project pursues several goals. Chief among them is verifying the ALEGRA magnetohydrodynamics code. We explore how reliable ALEGRA is in its static limit. By the static limit we understand the stationary states without macroscopic current. We choose quite a general class of 2-dimensional static solutions for which a linear isotropic metallic ellipse is placed inside a stationary magnetic field approaching a constant value H_i° at infinity. The flexible, convenient closed-form solutions for the interior of the inclusion provide a useful basis for verification of numerical methods.
The second goal is not computational but physical – it is to explore in the quasi-static approximation the process of evolution of the magnetic fields inside and outside the inclusion and the parameters for which the quasi-static approach provides for self-consistent results. We demonstrate that under spatial mesh refinement, ALEGRA converges to the analytic solution for the interior of the inclusion at the expected rate, for both body-fitted and regular rectangular meshes.

15. SUBJECT TERMS
magnetism, magnetohydrodynamics, permeability, verification

16. SECURITY CLASSIFICATION OF:			17. LIMITATION OF ABSTRACT	18. NUMBER OF PAGES	19a. NAME OF RESPONSIBLE PERSON
a. REPORT	b. ABSTRACT	c. THIS PAGE			Michael Grinfeld
Unclassified	Unclassified	Unclassified	UU	40	19b. TELEPHONE NUMBER (Include area code) 410-278-7030

Standard Form 298 (Rev. 8/98)
Prescribed by ANSI Std. Z39.18

Contents

List of Figures

Acknowledgments

Special thanks to Steven Segletes for a very helpful LaTeXtypesetting configuration, and to Allen Robinson and Chris Siefert (Sandia National Laboratories) for helpful technical insights relating to transient magnetics analysis and computation.

1. Introduction

ALEGRA is a multipurpose computational tool for modeling a variety of mechanical and electromagnetic phenomena and their interplay. This multiphysics capability is a key feature of ALEGRA and the result of many years of multidisciplinary effort. However, it carries with it a necessarily high cost for validation and verification (V&V). Fortunately, V&V efforts can take advantage of the compartmentalization ingrained in the architecture of ALEGRA. In other words, various modules of ALEGRA can be used without others when necessary. Therefore, the V&V procedures can be compartmentalized as well.

In this report, we study the reliability of ALEGRA's transient magnetics module for the static limit, and we explore the quasi-static evolution through which a steady state solution is reached for a particular problem of interest. We begin in Section 2 by reviewing the system of equations used to describe quasi-static magnetization. For the reader's convenience, an analytic solution is presented here in summary form for the problem of interest in the project. In Section 3, the full derivation of this solution is presented in detail. This section may be skipped in the first reading of the report. Section 4 provides some important information on the system of units to be used. Section 5 describes the ALEGRA code. Section 6 describes the configuration of the ALEGRA simulations. In Section 7, the qualitative behavior of the computed solution over time is described and illustrated graphically. The quantitative verification analysis appears in Section 8, followed by conclusions in Section 9.

2. The Quasi-Static Theory of Polarization of Metals

In the theoretical part of this project we follow the classical textbook of theoretical physics.[1]

2.1 Master System

The analysis of quasi-statics is based on the following master system

$$z^{ijk}\nabla_j E_k = -\frac{1}{c}\frac{\partial B^i}{\partial t} \tag{1}$$

$$z^{ijk}\nabla_j H_k = \frac{4\pi}{c}J^i \tag{2}$$

$$J^i = \sigma^{ij}E_j \tag{3}$$

$$B^i = B^i\left(H^i\right) \tag{4}$$

These bulk partial differential equations (PDEs) should be augmented with the boundary conditions

$$\left[B^i\right]^+_- n_i = 0,\ \ \left[H_i\right]^+_- \tau^i = 0 \tag{5}$$

and appropriate conditions at infinity as well as with the corresponding initial conditions.

In the system 1-5, z^i and t are the spatial (Eulerian) coordinates and time; $E_i,\ H_i$ and B^i are the electric and magnetic field and magnetic induction, respectively; J^i is the electric current density of free charges, c is the speed of light in vacuum, σ^{ij} is electrical conductivity.

Subsystem 1, 2 comprises a correspondingly reduced classical Maxwell system for electromagnetic field. Equation 1 is Faraday's law. Equation 2 is Ampère's law, where displacement currents have been neglected. Equation 3 represents Ohm's law

in its the simplest linear version. The function $B^i\left(H^i\right)$ is the so-called constitutive equation for the magnetic field. The constitutive relations 3 and 4 should be derived from experiments. In order to avoid major physical errors these equations should be taken in such a way that the total master system 1-4 satisfies the First and Second laws of thermodynamics. These demands entail quite strong *a priori* constraints on the constitutive equations.

In the boundary conditions 5, n_i and τ^i are the normal and the tangent vectors to the discontinuity boundaries.

2.2 Notation

The metrics co- and contra-variant tensors z_{ij}, z^{ij} of the Eulerian coordinate system are used for lowering and raising ("juggling") the indexes, and for defining the covariant differentiation ∇_i with respect to the coordinates z^i; z^{ijk} is the so-called covariant Levi-Civita skew-symmetric tensor. Using tensorial notation permits one to present all the equations in the universal covariant (i.e., coordinate-independent) form. The same goal can be reached with the help of the so-called direct or coordinate-independent form, which in the pre-Einsteinian era was the most widespread in the electromagnetic literature. Further details on tensorial algebra and calculus can be found in a plethora of textbooks, including the most popular and practical.[2,3]

We assume the coordinate system z^i to be Cartesian. In the Cartesian coordinate system, the metrics tensors numerically coincide with the corresponding values of the Kronnekker symbol $\delta_{ij},\ \delta^{ij},\ \delta^i_j$. The Levi-Civita tensor z^{ijk} has the main component z^{123} equal to 1. Juggling of the indexes does not change the numerical values of tensor components. Nonetheless, we will place all of the indexes in the covariant manner, thus following the demand of mathematical aesthetics and simplifying the passage between different coordinate systems when necessary.

2.3 Vector Potential

The ALEGRA code uses the vector potential A_i. The vectors A_i and H_i are interconnected by the covariant differential relation

$$H^i = z^{ijk}\nabla_j A_k \tag{6}$$

With a known spatial distribution of the vector potential potential $A_k(z,t)$ one can immediately and explicitly recover the magnetic field H^i using the formula 6. The opposite is not true. First of all, to recover the potential A_k with the help of a known field H^i one has to solve the boundary value problem, based on the PDE 6. Equation 6 alone is insufficient for solving this inversion problem. In order to make the inversion unique one has to add to 6 one of the calibration conditions:

(a) the Coulomb gauge

$$\nabla^i A_i = 0 \tag{7}$$

or

(b) the (relativistically invariant) Lorentz gauge

$$\frac{1}{c}\frac{\partial \varphi}{\partial t} + \nabla^i A_i = 0 \tag{8}$$

where $\varphi(z,t)$ is the scalar potential of the electric field E_k.

2.4 System to be Solved

We proceed with the analysis of linear isotropic materials that are free of bulk electric charge or material magnetization, for which

$$\sigma^{ij} = \sigma z^{ij} \tag{9}$$

and

$$B^i = \mu H^i, \tag{10}$$

where μ is the magnetic permeability.

Eliminating J^i between 2 and 3, we get

$$z^{ijk}\nabla_j H_k = \frac{4\pi\sigma}{c}E^i \tag{11}$$

Eliminating E^i between 1 and 11, we get

$$\frac{\partial B^i}{\partial t} = \frac{c^2}{4\pi\sigma}\nabla_j \nabla^j_{\cdot} H^i_{\cdot} \tag{12}$$

or

$$\frac{4\pi\sigma\mu}{c^2}\frac{\partial H^i}{\partial t} = \nabla_j \nabla^j_{\cdot} H^i_{\cdot} \tag{13}$$

The "parabolic" equation 13 should be combined with the boundary conditions.

In the equilibrium, time-independent, configuration we get the following system:

$$\nabla_j \nabla^j_{\cdot} H^i_{\cdot} = 0 \tag{14}$$

whereas the boundary conditions can be rewritten as follows:

$$[\mu H_i]^+_- n^i = 0, \;\; [H_i]^+_- \tau^i = 0 \tag{15}$$

If the magnetic field H°_i at infinity is given, the system 15 has to be analyzed under the additional boundary condition at infinity

$$\underset{|\mathbf{z}|\to\infty}{H^i = B^i} \to H^{i\circ} = B^{i\circ} \tag{16}$$

2.5 Elliptic Inclusion

There are few exact 2-dimensional (2-D) and 3-dimensional (3-D) solutions of the system 14 - 16. One of them is a solution for an elliptic inclusion in an infinite isotropic matrix, in particular, in vacuum. This solution is described below.

Consider an ellipse with the semi-axes a and b coinciding with the Cartesian axes z^1 and z^2, as shown in Fig. 1. We assume that the elliptical domain is filled with a linear isotropic substance with magnetic permeability μ. We then assume that the ellipse is immersed in the unbounded space in which there is a uniform magnetic field $H^{i\circ}$.

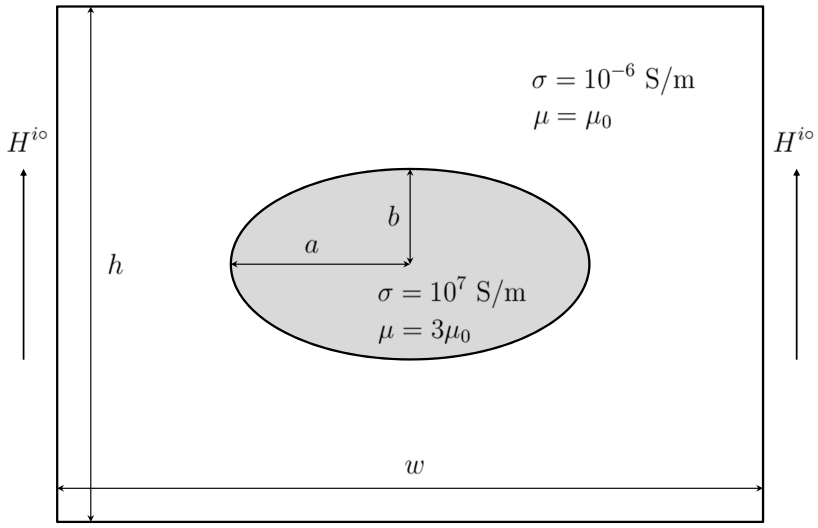

Fig. 1: Schematic diagram (not to scale) showing problem to be considered.

If there is an elliptical inclusion, the otherwise uniform field $H^i = H^{i\circ}$ will change. The changes are particularly strong inside the ellipse and in its vicinity. At infinity, the newly generated field H^i approaches its original value, $H^{i\circ}$.

2.6 Summary of Solution

Lengthy calculations show that the field H^i inside the ellipse is uniform, and it is given by the relationship

$$\left\| \begin{array}{c} H^1_{inside} \\ H^2_{inside} \end{array} \right\| = \left\| \begin{array}{c} \frac{a+b}{a+\mu b} H^\circ_1 \\ \frac{b+a}{\mu a+b} H^\circ_2 \end{array} \right\| \tag{17}$$

It should be noticed that this is a simple, elegant, closed-form expression that is very easily evaluated. Because it implies that the field inside the ellipse is *uniform*, it can even be used for quick visual, qualitative inspection of computed solutions.

The field H^i outside of the ellipse is given by the more complicated relationship

$$\left\| \begin{array}{c} H^1_{outside} \\ H^2_{outside} \end{array} \right\| = \tag{18}$$
$$\left\| \begin{array}{c} \frac{1}{2\pi}\frac{\partial^2\Theta}{\partial z^1 \partial z^1}\frac{(a+b)(\mu-1)}{a+\mu b}H_1^\circ + \frac{1}{2\pi}\frac{\partial^2\Theta}{\partial z^1 \partial z^2}\frac{(a+b)(\mu-1)}{\mu a+b}H_2^\circ + H_1^\circ \\ \frac{1}{2\pi}\frac{\partial^2\Theta}{\partial z^2 \partial z^1}\frac{(a+b)(\mu-1)}{a+\mu b}H_1^\circ + \frac{1}{2\pi}\frac{\partial^2\Theta}{\partial z^2 \partial z^2}\frac{(a+b)(\mu-1)}{\mu a+b}H_2^\circ + H_2^\circ \end{array} \right\|$$

where Θ is the logarithmic potential of the ellipse, given by the relationship:

$$\Theta(\mathbf{z}) = -\int\limits_{\omega^*_{ell}} d\omega \ln|\mathbf{z} - \mathbf{z}^*| \tag{19}$$

The full derivation of this solution is described in detail in the following section, which is included only for completeness. This section may be passed over in the first reading.

3. Full Derivation: Magnetization of Isotropic Elliptical Inclusion

This problem was analyzed by many outstanding mathematicians and physicists working on it since Newton's times. First, it was focused on various problems of gravitation and cosmology. Later on, in addition to mathematicians, the beauty of this problem hypnotized researchers exploring electromagnetism, theory of elasticity among others. Monographs[1,4,5]and papers[6,7] give a picture of various applications of this problem. In the presentation below we use the approach of Grinfeld,[8] which combines some techniques of Sretensky[4] and Eshelby.[6,7]

We will be seeking a solution $H_i = \eta_{i-}(z)$ inside the ellipse in the following form:

$$\eta_{i-}(z) = K_i \tag{20}$$

The solution in the form 20 automatically satisfies the PDE 14.

For the solution outside of the elliptic inclusion, the solution has the following form:

$$\eta_{i+}(z) = -W^j \nabla_j \nabla_i \Theta_+ + H_i^\circ \tag{21}$$

where Θ is the logarithmic potential of an ellipse.

The potential $\Theta(z)$ is defined in Equation 19 and satisfies the PDEs

$$\begin{aligned} \nabla_i \nabla^i \Theta &= -2\pi,\ z \in \omega_{ell}, \\ \nabla_i \nabla^i \Theta &= 0,\ z \in R^2/\omega_{ell} \end{aligned} \tag{22}$$

The solution in the form 21 automatically satisfies the PDE and the condition at infinity 16.

The potential inside the ellipse $\Theta_-(z)$ is described by the quadratic form

$$\Theta_-(z) = C - \frac{1}{2} Y_{ij} z^i z^j \tag{23}$$

where C is a constant, and Y_{ij} is a symmetric tensor depending on the shape of the ellipse and described below.

We turn now to the boundary conditions 15. First of all, we get

$$\nabla_i \nabla_j \Theta_+ = \nabla_i \nabla_j \Theta_- + [\nabla_i \nabla_j \Theta]_-^+ \tag{24}$$

Using the so-called compatibility condition

$$[\nabla_i \nabla_j \Theta]_-^+ = 2\pi n_i n_j \tag{25}$$

and the relationship 23, we can rewrite 24 as follows:

$$\nabla_i \nabla_j \Theta_{+0} = -Y_{ij} + 2\pi n_i n_j \tag{26}$$

Using 21 and 26, we can rewrite the boundary values $\eta_{i+0}(z)$ as follows:

$$\eta_{i+0}(z) = -W^j \nabla_j \nabla_i \Theta_{+0} + H_i^\circ = W^j \left(Y_{ij} - 2\pi n_i n_j\right) + H_i^\circ \tag{27}$$

The solution $\Theta_+(z)$ outside of the ellipse is much more complex. Fortunately, having known the solution inside the inclusion, that is, the constants C and Y_{ij}, we can uniquely recover the potential outside of the inclusion. Using the boundary conditions 18, 19, we can find all of these constants.

Again by luck, permitting one to find the exact solution is the fact that the boundary conditions 18, 19 require one to know the field $\Theta_\pm(z)$ not everywhere but only at the ellipse's interface Θ_{+0}.

We can rewrite the boundary conditions 14, 15 as follows:

$$\left(W^j Y_{ij} + H_i^\circ - K_i\right) \tau^i = 0 \tag{28}$$

and

$$\left\{\mu_- K_i - \mu_+ \left(W^j \left(Y_{ij} - 2\pi\delta_{ij}\right) + H_i^\circ\right)\right\} n^i = 0 \tag{29}$$

Since conditions 28, 29 should be satisfied for arbitrary orientations of the vectors τ_i and n^i, the system 28, 29 implies

$$K_i - W^j Y_{ij} = H_i^\circ \tag{30}$$

and

$$\mu_- K_i - \mu_+ \left(Y_{ij} - 2\pi\delta_{ij}\right) W^j = \mu_+ H_i^\circ \tag{31}$$

Using 30, we can rewrite 31 as follows:

$$\left(\mu_- - \mu_+\right) K_i + 2\pi W_i = 0 \tag{32}$$

as implied by the chain

$$\begin{aligned} \mu_- K_i - \mu_+ \left(Y_{ij} W^j - 2\pi \delta_{ij} A^j \right) &= \mu_+ H_i^\circ \rightarrow \\ \mu_- K_i - \mu_+ \left(K_i - H_i^\circ - 2\pi \delta_{ij} W^j \right) &= \mu_+ H_i^\circ \rightarrow \\ K_i \left(\mu_- - \mu_+ \right) + 2\pi W_i &= 0 \end{aligned} \tag{33}$$

In the case of a body immersed in vacuum ($\mu_+ = 1$ for Gaussian units) the relationship 32 reads

$$\left(\mu_- - 1 \right) K_i + 2\pi W_i = 0 \tag{34}$$

Summarizing, we have arrived at 2 linear vectorial Equations 30, 34 with 2 unknowns K_i and W_i. Excluding W_i between these 2 equations, we get a single vectorial equation:

$$\left(\delta_{ki} + Y_{ki} \frac{\mu_- - 1}{2\pi} \right) K^k = H_i^\circ \tag{35}$$

After solving Equation 35 with respect to K^k we can find W_i from the equation

$$W_i = -\frac{1}{2\pi} \left(\mu_- - 1 \right) K_i, \tag{36}$$

thus finishing the determination of the exact solution.

In the coordinate system whose axes coincide with the axes of ellipse, the geometric tensor Y_{ki} has the following components

$$\| Y_{ki} \| = \left\| \begin{array}{cc} Y_{11} & Y_{12} \\ Y_{21} & Y_{22} \end{array} \right\| = \frac{2\pi}{a+b} \left\| \begin{array}{cc} b & 0 \\ 0 & a \end{array} \right\| \tag{37}$$

Thus, we can rewrite the system 37 as follows

$$\begin{Vmatrix} 1+\frac{b}{a+b}(\mu-1) & 0 \\ 0 & 1+\frac{a}{a+b}(\mu-1) \end{Vmatrix} \times \begin{Vmatrix} K_1 \\ K_2 \end{Vmatrix} = \begin{Vmatrix} H_1^\circ \\ H_2^\circ \end{Vmatrix}$$

or

$$\begin{Vmatrix} \frac{a+\mu b}{a+b} & 0 \\ 0 & \frac{b+\mu a}{a+b} \end{Vmatrix} \begin{Vmatrix} K_1 \\ K_2 \end{Vmatrix} = \begin{Vmatrix} H_1^\circ \\ H_2^\circ \end{Vmatrix} \tag{38}$$

The system 38 has the following solution:

$$\begin{Vmatrix} K_1 \\ K_2 \end{Vmatrix} = \begin{Vmatrix} \frac{a+b}{a+\mu b}H_1^\circ \\ \frac{b+a}{\mu a+b}H_2^\circ \end{Vmatrix} \tag{39}$$

and

$$\begin{Vmatrix} W_1 \\ W_2 \end{Vmatrix} = \begin{Vmatrix} -\frac{1}{2\pi}\frac{(a+b)(\mu-1)}{a+\mu b}H_1^\circ \\ -\frac{1}{2\pi}\frac{(a+b)(\mu-1)}{\mu a+b}H_2^\circ \end{Vmatrix} \tag{40}$$

thus reproducing Equation 17. Then, inserting the relationships 40 of W_1 and W_2 in Equation 21, we arrive at Equation 18.

4. The Master System in the SI

So far our analysis relied on the usage of the Gauss system of electromagnetic units. On the other hand, the "magnetohydrodynamics" (MHD) module of the ALEGRA code uses only Système International (SI) units. Each of the systems has its own pros and contras. Before discussing the ALEGRA results, let us first rewrite the master system 1-5 using SI units. We get

$$z^{ijk}\nabla_j E_k = -\frac{\partial B^i}{\partial t} \tag{41}$$

$$z^{ijk}\nabla_j H_k = J^i \tag{42}$$

In the case of a linear isotropic medium that is free of bulk electric charge or material magnetization, we still have the relationships

$$B^i = \mu H^i \tag{43}$$

and

$$J^i = \sigma E^i \tag{44}$$

Boundary conditions are given by

$$\left[B^i\right]^+_- n_i = 0, \;\; [H_i]^+_- \tau^i = 0 \tag{45}$$

We note that in SI units, the vacuum permeability is given by the fundamental constant $\mu_0 = 4\pi \times 10^{-7}$ N/A^2. For regions exterior to the ellipse, $\mu = \mu_0$.

5. ALEGRA Formulation

The system 41-43 is a form of the equations solved by the "transient magnetics" module of the ALEGRA code.[9,10] In this module, the time evolution of electromagnetic fields in a stationary conducting medium is computed in quasi-static fashion. The system can be obtained from Maxwell's equations by use of the so-called "magneto-quasi-static" approximation.[11]

Electromagnetic radiation and separation of charges are not possible in the medium under this approximation. This can be understood by the absence of Maxwell's displacement current from Equation 42, and the absence of Gauss's law (relating the electric displacement to the charge density) from the system completely. The divergence-free character of the magnetic field is implied in Equation 45.

The medium is assumed to be both stationary and electrically neutral in the "transient magnetics" module. Mechanical and electromagnetic forces are not applied, and the thermodynamic state (internal energy) of the material is not updated. An implicit linear solver (see Section 6) is used to solve the system with an unstructured 2-D or 3-D finite-element discretization, and evolve the solution forward in

time. (Only quadrilaterals are considered here, although triangles are possible for the "transient magnetics" module.) Specialized "algebraic multigrid" methods are used to ensure sufficient scalability of the solve operation for large meshes (more than 10^5 elements) and parallel processing.

ALEGRA is equipped to handle – and has been used successfully for – a much broader class of problems.[10,12–14] These include deforming solid and hydrodynamic media, mechanical and electromagnetic forces, and adiabatic and Ohmic sources of heating, via its "magnetohydrodynamics" (MHD) module. The MHD physics module couples the transient magnetics capabilities with the continuum mechanics capabilities that form ALEGRA's basis, enhanced to incorporate electromagnetic induction and conservation of magnetic flux. Thus, the insights gained from this study should apply to those problems, since the transient magnetics capabilities are used in coupled fashion in those types of calculations.

To obtain a simple transient magnetics simulation in ALEGRA, with the limitations described above, it is only necessary to use the "transient magnetics" keyword in the input as the name of the physics module to be employed. ALEGRA solves either the system 41-43, or the system recast in terms of the vector potential A_i, depending on the configuration of the problem. For the problem considered here, the geometry is such that ALEGRA solves the system in terms of the out-of-plane component of the vector potential, which we refer to as A. The magnetic flux density B_i is then a derived variable.

6. Simulation Development

Two-dimensional ALEGRA transient magnetics simulations were run for the problem described in Section 2 and Fig. 1. In particular, we considered the situation where $a = 1.8$ cm, $b = 0.56$ cm, and $H^\circ = (0, 1/\mu_0)$ Ampere/m. This is an ellipse with an eccentricity of 0.831 and an aspect ratio of 3.24. We used a rectangular simulation domain with horizontal dimension $w = 30$ cm and vertical dimension $h = 15$ cm. For the ellipse, a contrived material was used, with a relative permeability μ = 3.0 and a constant isotropic electrical conductivity of σ = 10^7 S/m. Since all forces and heating are neglected in transient magnetics, the density and temperature of the material are fixed at their arbitrary initial values. For these conditions, the exact solution given in Equation 17 is predicts an equilibrium magnetic induction $B_1 = 0$ and $B_2 = 1.18657$ T in the ellipse interior.

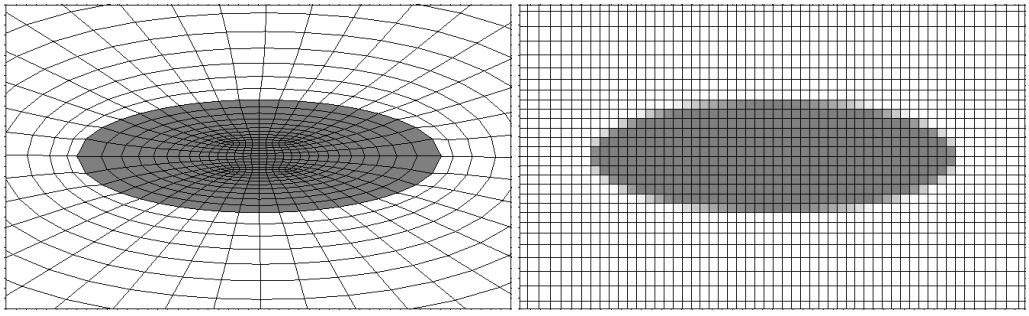

Fig. 2: Zoomed-in view of meshes used for ALEGRA simulations: body-fitted (left) and regular (right).

6.1 Spatial Discretization

Two mesh configurations were used: (1) a body-fitted irregular mesh representing an ideal best-case simulation with no multimaterial elements, and (2) a regular rectangular mesh with multimaterial elements representing a more typical production use case for ALEGRA. In the latter configuration, the elliptical shape is captured only in volume fraction information. The 2 mesh configurations are shown in Fig. 2, with the view zoomed in to show detail in the region of the ellipse. Mesh biasing was used in the regular case to coarsen the mesh at large distances exterior to the ellipse and concentrate computational effort within it and nearby; the regular mesh bias aspect ratio was limited to a maximum of 4.

The meshes shown in Fig. 2 were chosen to provide roughly the same number of elements inside the ellipse. This was achieved by assigning $N = 32$ elements around the perimeter of the ellipse in the body-fitted case, and $N = 40$ elements across the major (horizontal) axis in the regular case. However, for the regular mesh, roughly 10 times more elements were required to discretize the remainder of the domain than for the body-fitted mesh, even with mesh biasing. This made the regular-mesh calculations much more costly than the body-fitted mesh calculations.

6.2 Time Discretization

The "transient magnetics" capability in ALEGRA uses an implicit solver, and therefore does not place stringent restrictions on the choice of timestep size. For this study, the time evolution of the system during relaxation to equilibrium is of interest, so a very short, fixed timestep $dt = 2$ μs was still used.

The time required for the system to reach equilibrium can be approximated using

a scaling relationship that arises from the 1-dimensional (1D) magnetic diffusion equation,[5] giving a magnetic diffusion time $\tau_d \approx \mu\sigma\ell^2$, where ℓ is a characteristic length scale. Using the shortest dimension of the ellipse ($b = 0.56$ cm), we obtain $\tau_d \approx 1.2$ ms as the time for one e-fold increase of the field soaking into the ellipse. Therefore, the simulations were run out to a termination time of 0.01 seconds (s), to capture the full relaxation to equilibrium by observing 8 e-foldings.

6.3 Solver

The implicit iterative solver used for transient magnetics in ALEGRA is the AztecOO solver[15] from the Trilinos package.[16] The algebraic multigrid ("multilevel") capabilities included in the solver were enabled here, so that maximum throughput could be obtained on the larger calculations, and the actual conditions used in typical production MHD calculations with ALEGRA could be reproduced. Through the AztecOO interface, a conjugate gradient solver type was specified, with an iteration stopping tolerance of 10^{-16}.

6.4 Initial and Boundary Conditions

The ALEGRA simulations were initialized to the configuration shown in Fig. 1, with zero magnetic field (and thus zero current) everywhere in the domain. The system becomes magnetized because of a uniform y-oriented source magnetic field imposed on the left and right boundaries, which is assumed to be switched on instantaneously at time zero. The component of the magnetic field H^i tangent to the mesh is fixed on the left and right boundaries, so that over the course of the simulation, the solution relaxes to an equilibrium state, which is equivalent to the equilibrium condition described in Section 2. On the top and bottom boundaries, the tangent component of H^i is constrained to be zero, so that field lines are normal to the boundary there.

Explicit boundary conditions on the material interfaces are not needed. The material discontinuity is represented in the calculation as a discontinuity in σ and μ. In multimaterial elements, mean values of these properties are used.

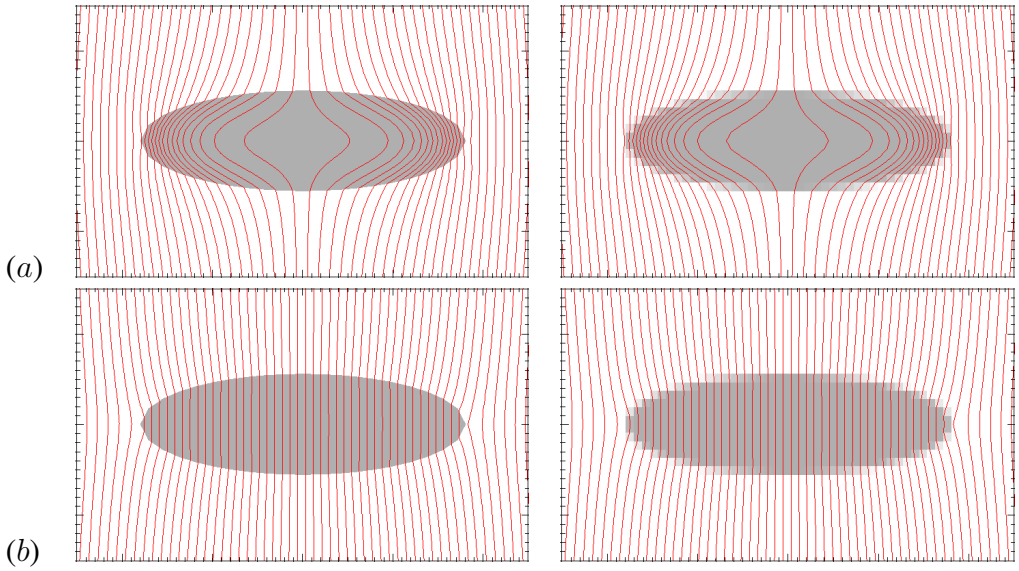

Fig. 3: Configuration of B^i field lines before a) and after b) after the equilibrium state is reached, for the body-fitted (left) and regular (right) mesh types. Simulation times: a) 0.2 ms, b) 3.0 ms.

7. Time Evolution of the System

In the ALEGRA simulations, the evolving variables are the in-plane magnetic induction vector B^i, the in-plane magnetic field H^i, the out-of-plane magnetic vector potential A, and the out-of-plane electric current density J. The latter 2 vectors are constrained to have only a z component, so are treated by the code as scalar quantities.

The code also computes a total electric current I, which is a positive quantity obtained from surface integrals of J. The total surface integral is zero by construction; this can be seen by taking the divergence of Equation 42. The magnitude of opposed currents running transiently in the conductor normal to the plane is obtained by isolating the positive and negative contributions to the total surface integral, which should be equal.

Over the course of the simulation, the current I and time derivatives of H^i, B^i, and A all relax toward zero as magnetic diffusion proceeds toward a "saturated" or equilibrium field configuration. Magnetic field lines computed by ALEGRA before and after equilibrium is reached are shown for both mesh types in Fig. 3. The lines are obtained conveniently in practice by plotting contours of A. In the system

considered here, with $\mu \neq \mu 0$, the equilibrium field configuration is nonuniform. As predicted in Section 2, it is only uniform in the interior of the inclusion late in time. The uniform interior field configuration has visibly not been reached yet by $t = 0.6$ μs, as seen in Fig. $3a$.

The evolution of the magnitude of B^i and J in the ALEGRA simulations is depicted in Figs. 4 and 5. We observe that the field "soaks" into the ellipse nonuniformly. Before the equilibrium value is reached, the local magnitude of the field first transiently rises to much larger values on the extreme horizontal limbs of the ellipse. The field magnitude near the center of the ellipse remains small until these transients decay, leading to a uniform vertically oriented interior field.

Fig. 4 shows results for the body-fit mesh, and Fig. 5 shows results for the regular mesh. Mesh lines are superimposed in both cases in the region of the ellipse. In the regular-mesh case, mesh lines are plotted for material volume fraction $f \geq 0.5$, with the estimated contour of $f = 0.5$ appearing as well. It should be noted that this contour does not represent a mesh line, but a post-processing contour estimate.

Comparing the body-fitted and regular-mesh results, we see that there are advantages and disadvantages to both approaches. A much stronger discontinuity in the solution variables is possible at the material interface in the body-fitted case, allowing greater accuracy. This greater accuracy is enormous for this coarse mesh size. However, the elements are much more distorted, allowing other errors to enter.

The primary advantage of the body-fit approach is that a much smaller total number of elements is required for this simulation domain: only about 900, compared to over 11,000 for the regular case. This allows computational effort to be concentrated in the region of interest (the ellipse). The smaller element count results in a much shorter simulation turnaround time: the body-fitted case runs to completion (in serial, for this coarse mesh size) in about 15% of the time required for the regular-mesh case (see table in Section 8).

The accuracy per-unit-compute-time is enormously greater with a body-fitted mesh. However, in most production calculations, a body-fitted mesh is not a viable option. Therefore, we have retained both mesh types in this study.

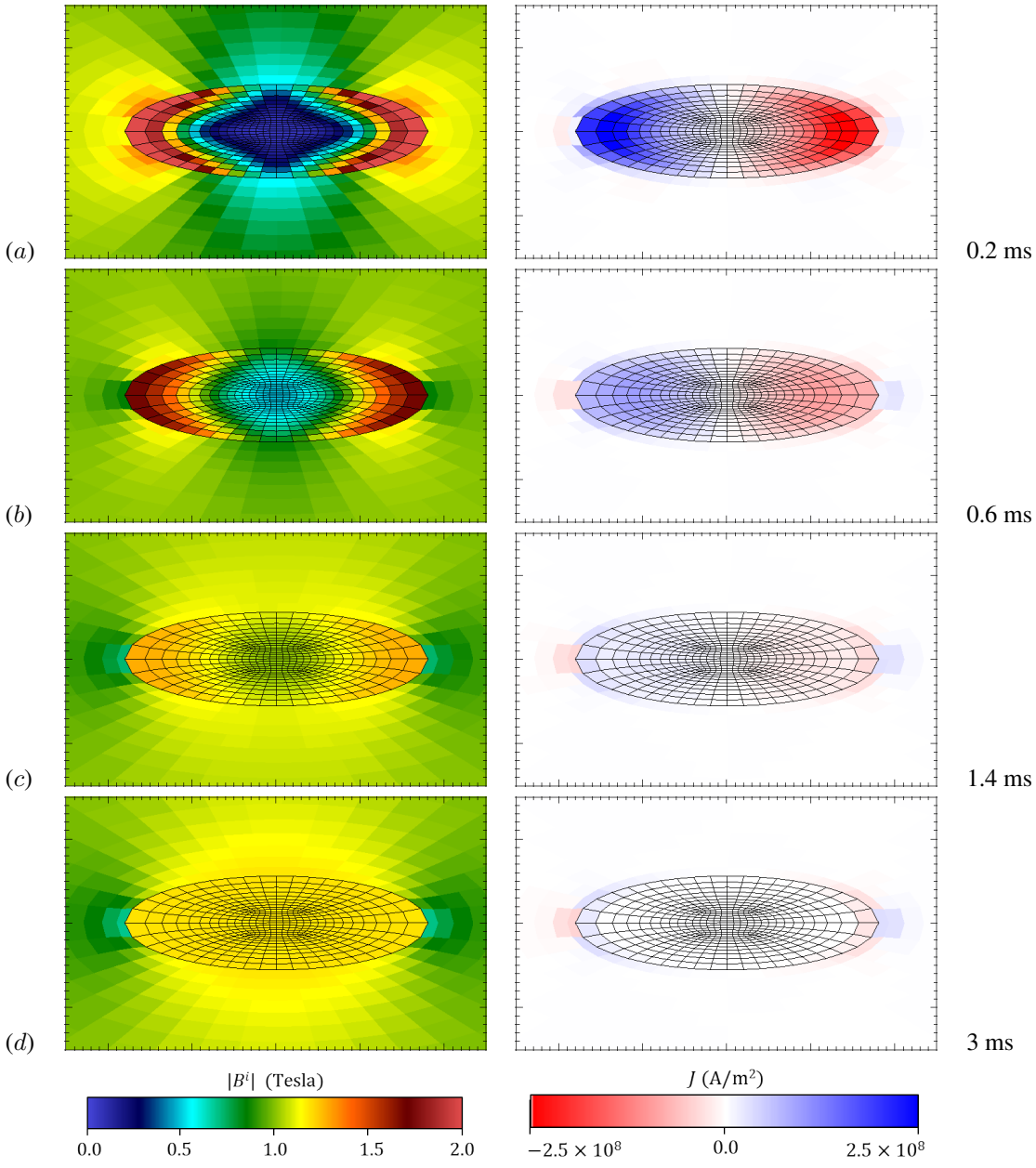

Fig. 4: Simulation evolution for body-fitted mesh: B^i magnitude (left) and J magnitude (right), with mesh lines in the ellipse superimposed. Simulation times: a) 0.2 ms, b) 0.6 ms, c) 1.4 ms, d) 3 ms. Blue-red colorbar for B^i spans $0 \leq |B^i| \leq 2$ T.

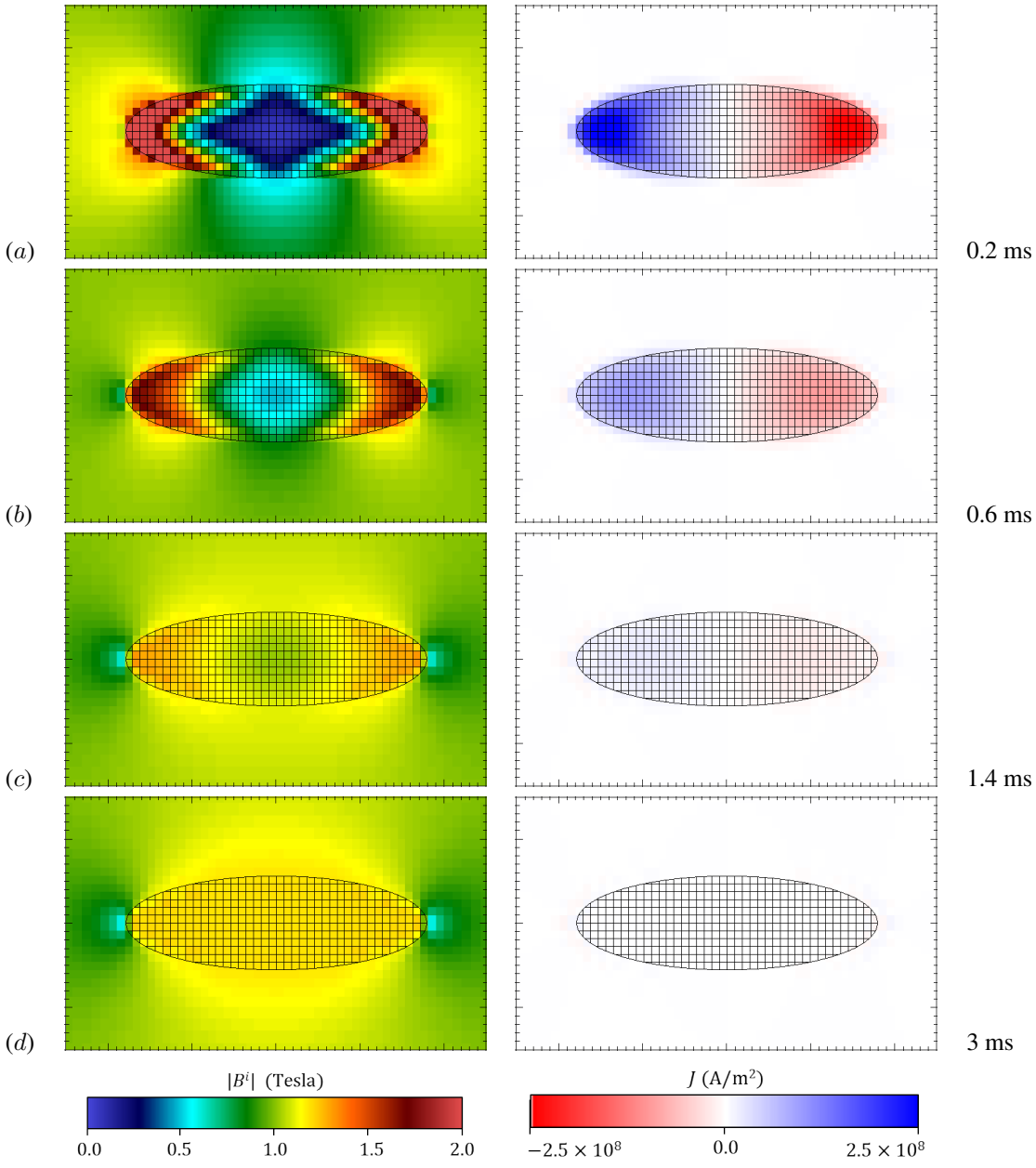

Fig. 5: Simulation evolution for regular mesh: B^i magnitude (left) and J magnitude (right), with mesh lines in the ellipse superimposed. Simulation times: a) 0.2 ms, b) 0.6 ms, c) 1.4 ms, d) 3 ms. Blue-red colorbar for B^i spans $0 \leq |B^i| \leq 2$ T.

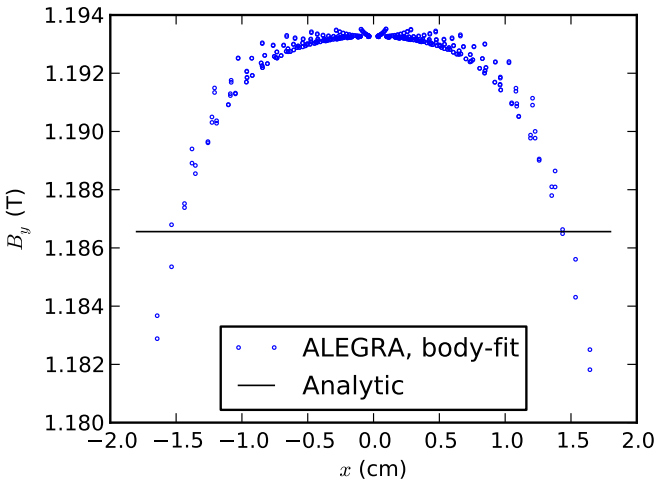

Fig. 6: Spatial distribution of deviation from exact solution for B_2 at equilibrium for body-fitted mesh with $N = 40$.

8. Solution Verification

The interior solution at $t = 0.01$ s was compared to the equilibrium solution given by Equation 17, which predicts $B_2 = 1.18657$ T. In the case of the regular mesh, only elements with $f \geq 0.5$ were considered in the comparison. Since B_2 is a derived variable in ALEGRA, and numerical differentiation is involved in computing its value, some additional inaccuracy is involved in the comparison. The fundamental variable in these calculations is A, but comparison was not done for A here, because in production calculations, the vector B^i is typically of principal interest. Nevertheless, even for B_2, we expect a reasonable qualitative match to the exact solution, and at least first-order convergence toward the solution under spatial mesh refinement, based on the methods implemented in ALEGRA, and the mesh types used here.[17]

8.1 Coarse-Mesh Comparison

Comparison of the equilibrium distribution of B_2 in the ellipse for the 2 mesh types shows that for the $N = 40$ case, which is a very coarse mesh requiring only minutes of serial compute time, ALEGRA matches the exact solution from Equation 17 to within fractions of a percent. The distributions computed on the $N = 40$ regular and body-fitted mesh types are shown with the exact solution in Figs. 6 and 7. The field is not perfectly uniform, but deviates from the uniform exact solution by only 0.02% for the body-fitted case and by only 0.1% for the regular case.

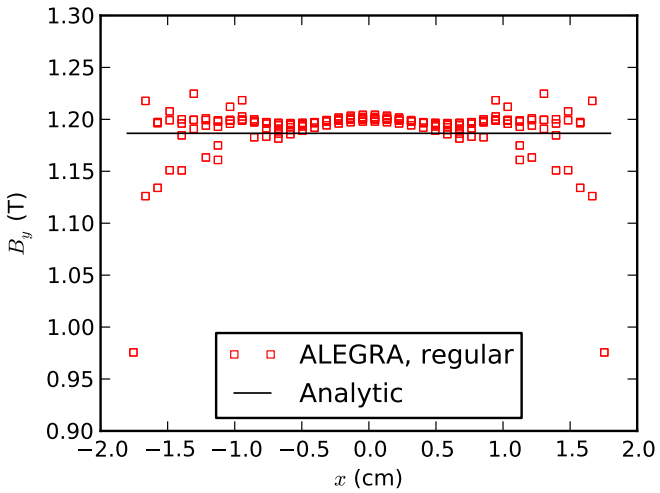

Fig. 7: Spatial distribution of deviation from exact solution for B_2 at equilibrium for regular mesh with $N = 40$.

The largest deviations appear on the horizontal limbs of the ellipse, particularly in the regular-mesh case. This suggests that greater inaccuracies are likely for elliptical inclusions with greater aspect ratios than 3.24 (see Section 8 below). The deviations are also much larger for the regular mesh than the body-fitted mesh at this mesh size because of the effect of mixed elements near the ellipse surface. At the center of the ellipse, the field magnitude exceeds the analytic value. Further analysis shows that the mean value of the computed field in the ellipse does slightly exceed the analytical value, as suggested by Figs. 6 and 7.

The global deviation from the exact solution was computed by summing the square of the local deviation over all locations inside the ellipse ($f \geq 0.5$), and normalizing by the tally of elements inside the ellipse. Taking the root then yields a root-mean-square (RMS) measure of the error in the computed $B-2$ distribution. Normalizing again by the value of the exact solution yields a fractional error.

This fractional error metric is plotted against time in Fig. 8 for the $N = 40$ case. We observe again that the body-fitted result is significantly more accurate at this mesh size. Further, we see that the error trend in both cases goes through a minimum during the transient phase, marking the moment when the average value of the field in the initially ellipse first surpasses the analytic value. The error reaches a plateau after about $t = 5$ ms. Also at about $t = 5$ ms, the current ceases to change significantly in time, reaching its final small but nonzero value.

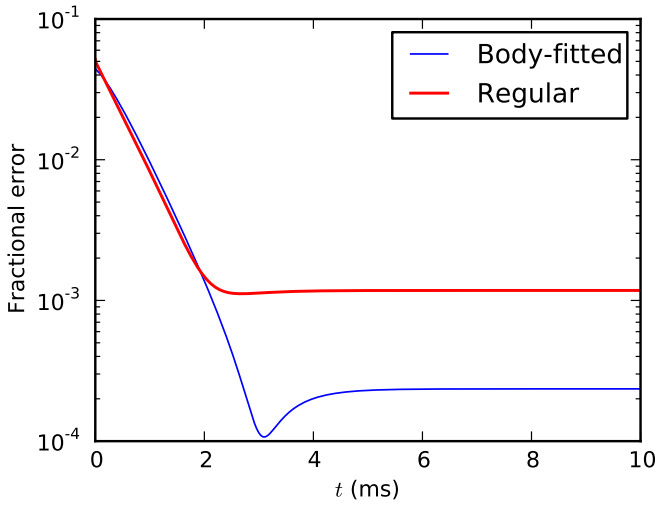

Fig. 8: Time evolution of RMS deviation of ALEGRA solution relative to exact solution for equilibrium condition at $N = 40$.

8.2 Convergence Under Spatial Refinement

Spatial-refinement convergence studies were also performed for both mesh types, starting from the coarse mesh shown in the foregoing discussion. Previous verification work for transient magnetics in ALEGRA has shown good convergence behavior in 3-D.[14,17] Here, the 2-D mesh interval was halved 5 times, yielding 6 resolution levels at $N = 40, 80, 160, 320, 640$, and $1,280$ elements per perimeter (body-fitted case) or elements per major axis (regular case) for comparison to the exact solution, using the fractional RMS error metric just described.

The error computed in this way from the series of simulations was observed to decay monotonically at approximately first order relative to the mesh interval. The error convergence trends are shown in Fig. 9. The trends are plotted against the total number of elements in the ellipse for each simulation, but convergence rates are computed against the value of N. We find average convergence rates of 0.9 for the body-fitted meshes and 1.3 for the regular meshes.

We see that the transient magnetics module in ALEGRA computes solutions that converge smoothly toward the analytic solution at the expected rate. ALEGRA computes magnetic diffusion into an ellipse with linear magnetic permeability with demonstrated accuracy, and the expected convergence behavior.

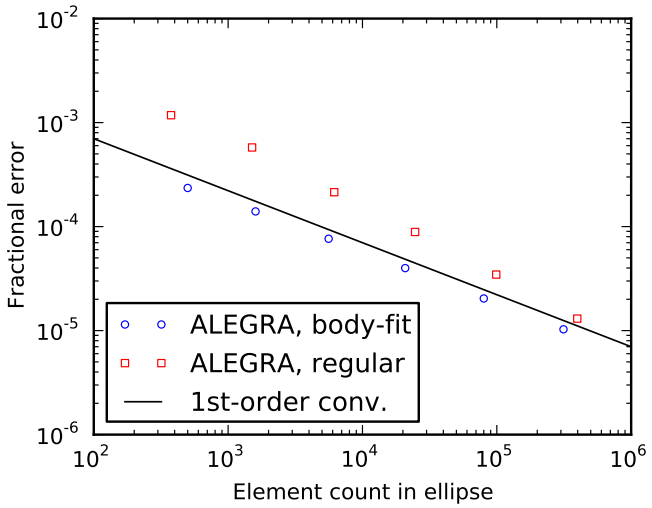

Fig. 9: Results of spatial mesh refinement convergence study for an elliptical inclusion, showing fractional error relative to exact solution.

Under spatial refinement, it becomes clear that the regular mesh approach with mixed elements is not as disadvantaged relative to body-fitted meshes as the $N = 40$ results indicate. Although the error magnitudes are larger for the regular mesh with mixed elements, the solution computed on these meshes converges at a much higher rate. Its convergence rate also improves as the mesh is refined. At the very largest meshes, the error magnitudes are comparable. Thus, there is a tradeoff between regular and body-fitted meshes, exchanging accuracy for convergence.

8.3 Aspect Ratio Effect

Since the performance of ALEGRA for a range of aspect ratios is also of interest, the spatial mesh refinement study was repeated for 2 more geometries: a circular inclusion, and an elliptical inclusion with an aspect ratio of 10. In the case of a circular inclusion, the dimensions $a = b = 1$ cm were used, with domain dimensions $w = h = 20$ cm. Otherwise the parameterization and analysis were the same. The exact solution for this case predicts an equilibrium vertical magnetic induction of $B_2 = 1.5$ T in the interior of the circle. Body-fitted and regular meshes were used, with the same series of mesh refinements.

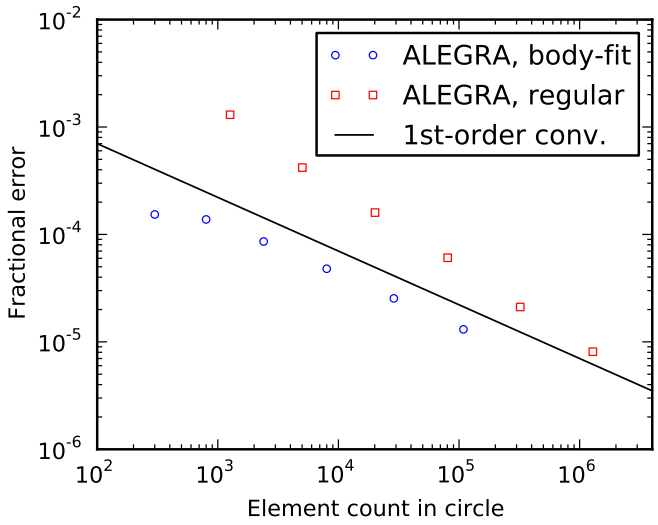

Fig. 10: Results of spatial mesh refinement convergence study for a *circular* inclusion, showing fractional error relative to exact solution.

Results for the circular case are shown in Fig. 10. Not surprisingly, the error magnitudes are for the most part lower for this simpler case, at each value of N. We also again observe larger error magnitudes but greater convergence rates for the regular mesh than for the body-fitted mesh. Further, the disparity in convergence rates also remains. The regular-mesh case converges at a mean rate of 1.5, while the body-fitted case at only 0.7.

To simulate an ellipse with aspect ratio $AR = 10$, dimensions $a = 3.16$ cm and $b = 0.316$ cm were used, with domain dimensions $w = 50$ cm and $h = 20$ cm. This corresponds to an eccentricity of 0.949. The exact solution for this case predicts an equilibrium vertical magnetic induction of $B_2 = 1.06452$ T in the interior of the ellipse. For this large aspect ratio, the meshing technique used to produce the elliptical body-fitted meshes was not operable due to the large mesh deformations required. Hence, no body-fit-mesh cases were studied. Further, in the regular-mesh case, a lower-accuracy geometry insertion method ("diatom, insert UDS" rather than "insert UDS+") had to be used, because of the high curvature of the shape.

Convergence results for the $AR = 10$ case are shown in Fig. 11, along with the results from the $AR = 3.24$ and $AR = 1$ cases discussed above with regular meshes. Here the fractional error is plotted as a function of N, not the number of elements in the ellipse.

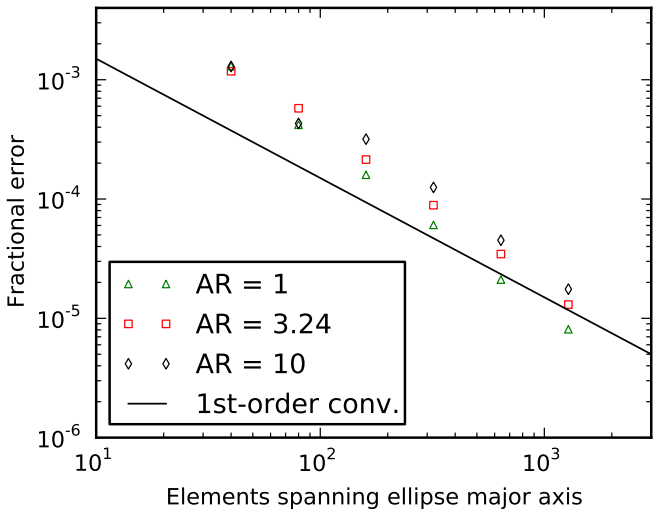

Fig. 11: Results of spatial mesh refinement convergence study for elliptical inclusions with various aspect ratios, showing fractional error relative to the respective exact solution as a function of N, for regular-mesh simulations.

For $AR = 10$, the computed solution converges less smoothly, and the error magnitudes are larger than for smaller aspect ratios. However, the solution converges at a mean rate of 1.2, which still compares favorably with the convergence rates for the circular inclusion (1.5) and the original elliptical inclusion (1.3). This suggests that with the regular-mesh setup, ALEGRA's accuracy for this problem should be preserved even for ellipses with very great eccentricity.

8.4 Compute Times

As a final note, some diagnostic data from the simulations for aspect ratio 3.24 are provided in the table, to illustrate the disparity in computational cost for the body-fitted and regular mesh scenarios. This includes the number of elements in the mesh, the number of compute cores used for each simulation, and the "wall-clock" time required for the ALEGRA calculation to run. The regular-mesh simulations required $10\times$ more elements at each value of N, resulting in a much lower rate of throughput, due to higher AztecOO solve times.

Despite the apparent lower rate of throughput for the regular-mesh cases, there are 2 mitigating factors. The body-fitted cases all carried fewer mesh elements per compute core, by about a factor of 2. Also, the body-fitted cases all required additional compute time to generate the mesh. The mesh-generation process does not lend itself to parallelization, and for the larger meshes required more time than the ac-

N	N_{elem} Body-fit	N_{elem} Regular	n_{cores} Body-fit	n_{cores} Regular	Wall time (s) Body-fit	Wall time (s) Regular
40	1.30×10^3	1.12×10^4	2	1	9.20×10^1	8.30×10^2
80	4.80×10^3	4.58×10^4	2	4	2.26×10^2	1.29×10^3
160	1.84×10^4	1.85×10^5	4	8	5.53×10^2	3.76×10^3
320	7.20×10^4	7.42×10^5	8	16	1.27×10^3	9.32×10^3
640	2.85×10^5	2.98×10^6	16	32	3.61×10^3	2.22×10^4
1280	1.13×10^6	1.19×10^7	32	64	9.31×10^3	6.62×10^4

Table: Diagnostic data from simulations run in spatial-refinement convergence study.

tual ALEGRA calculation. The expense of this operation mainly has to do with the Laplacian smoothing operation that had to be used to improve the symmetry of the quadrilateral mesh; this operation might not be required for triangular meshes. This is a significant drawback to using the body-fitted mesh approach.

9. Conclusions

This study has yielded several outcomes that should be useful for those interested in understanding the quasi-static behavior of magnetic fields in a medium that includes conducting, permeable materials.

First, a flexible and convenient analytic solution has been derived that describes the equilibrium field in the interior of an inclusion in such a medium that has a generic shape: an ellipse. Although the solution is rather complex outside the ellipse, inside the ellipse, it has a simple, closed form which lends itself well to verification of computed solutions by both visual inspection and convergence analysis. A similar static solution is valid in the electrostatic context.

Second, it has been shown that the equilibrium state can be reached by transient means via computation with ALEGRA, which allows the magnetic field to evolve by solving an initial-boundary-value problem that includes linear magnetic permeability in the inclusion. The time to reach the equilibrium state matches the magnetic diffusion time expected for the system based on its geometry and the material properties. This approach opens a novel venue for solving classical problems of magnetostatics and electrostatics of dielectrics.

Third, it has been demonstrated that the equilibrium state computed by ALEGRA

for this system reliably reproduces the analytic solution quite well, with errors on the order of 10^{-3} to 10^{-5} for reasonable compute times. Further, the solution converges under spatial refinement, and the convergence properties are preserved even for ellipse aspect ratios up to 10.

Finally, the results show that it is not necessarily more advantageous to use body-fitted meshes when simulating this system in ALEGRA on a quadrilateral mesh. For coarse meshes, the body-fitted approach does provide much greater accuracy and faster throughput. But as the mesh is refined, the advantage in accuracy slowly vanishes, and the cost of generating the body-fitted mesh becomes excessive, and even prohibitive for large ellipse aspect ratios. At all mesh sizes, the convergence rate on regular meshes surpasses that of body-fitted meshes.

This work lays the foundation for future extension into other areas of interest. An analytic solution in three dimensions for an ellipsoidal inclusion is also possible, which can be compared to computed solutions from ALEGRA to test its 3-D transient magnetics capabilities. Electromagnetic forces, motion, and thermodynamic effects could also be incorporated, without introducing significant difficulties in ALEGRA. All of these are areas that could be explored in future analysis with fruitful results.

10. References

1. Landau LD, Lifshitz EM. Electrodynamics of continuous media. Pergamon Press; 1984. Chapter VII "Quasi-Static Electromagnetic Field".

2. Schouten JA. Tensor analysis for physicists. Dover; 2011.

3. McConnell AJ. Applications of tensor analysis. Dover; 2011.

4. Sretenskii LN. Theory of the Newton potential. Moscow-Leningrad; 1946. In Russian.

5. Jackson JD. Classical electrodynamics. Hoboken, NJ: John Wiley and Sons, Inc.; 1999.

6. Eshelby JD. The determination of the elastic field of an ellipsoidal inclusion, and related problems. Proc. Roy. Soc. A. 1957;241:376–396.

7. Eshelby JD. The elastic field outside an ellipsoidal inclusion. Proc. Roy. Soc. A. 1959;252:561–569.

8. Grinfeld MA. Thermodynamic methods in the theory of heterogeneous systems. Longman Sc. & Tech.; 1991.

9. Robinson AC et al.. ALEGRA: An arbitrary Lagrangian-Eulerian multimaterial, multiphysics code. In: ALEGRA: An Arbitrary Lagrangian-Eulerian Multimaterial, Multiphysics Code; 2008 January; Reno, Nevada. AIAA-2008-1235

10. Robinson AC, Garasi CJ. Three-dimensional z-pinch wire array modeling with ALEGRA-HEDP. Comp. Phys. Commun. 2004;164:408–413.

11. Melcher JR. Continuum electromechanics. Cambridge, MA: MIT Press; 1981.

12. Doney R, Vunni G, Niederhaus J. Experiments and simulations of exploding aluminum wires: validation of ALEGRA-MHD. Aberdeen Proving Ground, MD: Army Research Laboratory; 2010. Report No.: ARL-TR-5299.

13. Uhlig WC, Hummer CR. In-flight conductivity and temperature measurements of hypervelocity projectiles. Procedia Engineering. 2013;58:48–57; (Proceedings of the 12th Hypervelocity Impact Symposium).

14. Doney R. Inductance scaling of a helicoil using ALEGRA. Aberdeen Proving Ground, MD: Army Research Laboratory; 2013. Report No.: ARL-TR-6397.

15. Heroux M. AztecOO user guide. Albuquerque, NM: Sandia National Laboratories; 2004. Report No.: SAND2004-3796.

16. Heroux M, Bartlett R, Howle V, Hoekstra R, Hu J, Kolda T, Lehoucq R, Long K, Pawlowski R, Phipps E, Salinger A, Thornquist H, Tuminaro R, Willenbring J, Williams A. An overview of Trilinos. Albuquerque, NM: Sandia National Laboratories; 2003. Report No.: SAND2003-2927.

17. Siefert CM, Robinson AC. A fully implicit method for 3D quasi-steady state magnetic advection-diffusion. Albuquerque, NM: Sandia National Laboratories; 2009. Report No.: SAND2009-6091.

List of Symbols

a – Horizontal ellipse semi-major axis

AR – Ellipse aspect ratio

B_i – Magnetic induction vector

b – Vertical ellipse semi-minor axis

c – Speed of light

E_i – Electric field vector

H_i – Magnetic field vector

$H^{i\circ}$ – Magnetic field at infinity

h – Vertical dimension of simulation domain

J^i – Current density vector

μ – Material magnetic permeability

μ_0 – Magnetic permeability of free space

n_i – Unit normal vector

N – Number of elements spanning ellipse major axis or perimeter

σ – Isotropic material electrical conductivity scalar

σ^{ij} – Electrical conductivity tensor

t – time

τ_d – Magnetic diffusion time

τ_i – Unit tangent vector

Θ – Logarithmic potential

w – Horizontal dimension of simulation domain

z_{ijk} – Levi-Civita tensor

1 (PDF) DEFENSE TECHNICAL INFORMATION CTR DTIC OCA

2 (PDF) DIRECTOR US ARMY RESEARCH LAB RDRL CIO LL IMAL HRA MAIL & RECORDS MGMT

1 (PDF) GOVT PRINTG OFC A MALHOTRA

6 (PDF) LOS ALAMOS NATL LAB C BRONKHORST R GRAY A MISRA D PRESTON R LEBENSOHN A SAXENA

5 (PDF) DREXEL UNIVERSITY DEPT MEM B FAROUK N CERNANSKY DEPT MATHEMATICS P GRINFELD DEPT MAT SCI & ENGNG Y GOGOTSI G TUCKER

2 (PDF) CALIFORNIA INST TECHNOLOGY WA GODDARD, III S ZYBIN

1 (PDF) CARNEGIE MELLON UNIVERSITY A ROLLETT

9 (PDF) JOHNS HOPKINS UNIVERSITY K HEMKER N DAPHALAPURKAR K RAMESH J EL-AWADY M FALK L GRAHAM-BRADY T HUFNAGEL V NGUYEN M ROBBINS

1 (PDF) UNIVERSITY OF MARYLAND R ARMSTRONG

4 (PDF) MASSACUSETTS INST TECHNOLOGY M DEMKOWICZ R ABEYARATNE L ANAND D PARKS

3 (PDF) RUTGERS G WENG V DOMNICH R HABER

1 (PDF) GEORGIA INST TECHNOLOGY D MCDOWELL

1 (PDF) UNIV CALIFORNIA SAN DIEGO MA MEYERS

1 (PDF) UNIV CALIFORNIA SANTA BARBARA R MCMEEKING

5 (PDF) SANDIA NATIONAL LABORATORIES C GARASI J NIEDERHAUS S PETNEY A ROBINSON C SIEFERT

ABERDEEN PROVING GROUND

38 (PDF) DIR USARL
RDRL CIH S
J CAZAMIAS
RDRL WM
B FORCH
J MCCAULEY
RDRL WML H
B SCHUSTER
RDRL WMM
J BEATTY
RDRL WMM B
G GAZONAS
D HOPKINS
B LOVE
B POWERS
RDRL WMM E
J SWAB
RDRL WMM F
T SANO
M TSCHOPP
RDRL WMM G
J ANDZELM
RDRL WMP
S SCHOENFELD

ABERDEEN PROVING GROUND(continued)
RDRL WMP A
A PORWITZKY
W UHLIG
RDRL WMP B
C HOPPEL
S SATAPATHY
M SCHEIDLER
A SOKOLOW
T WEERASOORIYA
RDRL WMP C
R BECKER
S BILYK
T BJERKE
D CASEM
J CLAYTON
D DANDEKAR
M GREENFIELD
R LEAVY
J LLOYD
S SEGLETES
A TONGE
C WILLIAMS
RDRL WMP D
R DONEY
J RUNYEON
G VUNNI
C RANDOW
RDRL VTM
M HAILE